Oceanic control of multidecadal variability in an idealized coupled GCM

Q. Jamet, Thierry Huck, Olivier Arzel, J.-M. Campin, Alain Colin de Verdiere

Climate Dynamics manuscript No.
(will be inserted by the editor)

Oceanic control of multidecadal variability in an idealized coupled GCM

Quentin Jamet · Thierry Huck · Olivier Arzel · Jean-Michel Campin · Alain Colin de Verdière

Abstract Idealized ocean models are known to develop intrinsic multidecadal oscillations of the Meridional Overturning Circulation (MOC). Here we explore the role of ocean-atmosphere interactions on this low-frequency variability. We use a coupled ocean-atmosphere model set up in a flat-bottom aquaplanet geometry with two meridional boundaries. The model is run at three different horizontal resolutions (4°, 2° and 1°) in both the ocean and atmosphere. At all resolutions, the MOC exhibits spontaneous variability on multidecadal timescales in the range 30-40 yr, associated with the propagation of large-scale baroclinic Rossby waves

Q. Jamet · T. Huck · A. Colin de Verdière · O. Arzel

Laboratoire de Physique des Océans (UMR 6523 CNRS IFREMER IRD UBO)

Université de Bretagne Occidentale, UFR Sciences, 6 avenue Le Gorgeu

CS 93837, 29238 Brest Cedex 3, FRANCE

Tel.: (+33) 298-016509 ; Fax: (+33) 298-016468

E-mail: quentin.jamet@univ-brest.fr

J.-M. Campin

Department of Earth, Atmospheric and Planetary Sciences,

Massachusetts Institute of Technology,

77 Massachusetts Ave., Cambridge, MA 02139, USA

across the Atlantic-like basin. The unstable region of growth of these waves through the long wave limit of baroclinic instability shifts from the eastern boundary at coarse resolution to the western boundary at higher resolution. Increasing the horizontal resolution enhances both intrinsic atmospheric variability and ocean-atmosphere interactions. In particular, the simulated atmospheric annular mode becomes significantly correlated to the MOC variability at 1° resolution. An ocean-only simulation conducted for this specific case underscores the disruptive but not essential influence of air-sea interactions on the low-frequency variability. This study demonstrates that an atmospheric annular mode leading MOC changes by about 2 years (as found at 1° resolution) does not imply that the low-frequency variability originates from air-sea interactions.

Keywords Atlantic Multidecadal Oscillation · Air-sea interactions · NAO · Rossby waves · Idealized configuration

1 Introduction

The Atlantic Multidecadal Oscillation (AMO, Kerr, 2000) is a significant mode of natural variability (Delworth et al, 2007) seen in averaged Sea Surface Temperature (SST) over the North Atlantic. The AMO has a well-established impact on climatic conditions over Europe, North America and Africa (Folland et al, 1986; Enfield et al, 2001; Sutton and Hodson, 2005). Early studies describe the AMO as a mode of variability with a 50-70 yr period (Enfield et al, 2001; Knight et al, 2005), but more recent studies also highlight another mode of variability with a period of about 20-30 yr (Frankcombe et al, 2008; Frankcombe and Dijkstra, 2009; Chylek et al, 2011).

The Meridional Overturning Circulation (MOC) in the Atlantic transports warm water northward at the surface and colder water southward at depth, resulting in a net northward heat transport. Changes in MOC heat transport are thought to modulate North Atlantic SST on multidecadal timescales, thereby the AMO (Schlesinger and Ramankutty, 1994; Kushnir, 1994). Delworth et al (1993) have shown the existence of a multidecadal Atlantic MOC variability using the GFDL coupled model, and Knight et al (2005) linked this MOC variability to the surface SST anomalies defining the AMO.

There is still no consensus on the mechanism that generates this multidecadal climate variability in the North Atlantic, particularly regarding the role of the atmosphere (Liu, 2012). Several hypotheses have been proposed which include either ocean-atmosphere coupled modes (Timmermann et al, 1998; Weaver and Valcke, 1998), oceanic modes that are excited by atmospheric noise associated with synoptic weather (Griffies and Tziperman, 1995; Sévellec et al, 2009; Frankcombe et al, 2009), oceanic response to variable atmospheric forcing (Delworth and Greatbatch, 2000; Eden and Jung, 2001; Eden and Willebrand, 2001), or intrinsic oceanic modes where the energy source originates from an internal instability of the large-scale ocean circulation (Colin de Verdière and Huck, 1999; Te Raa and Dijkstra, 2002).

The progress in understanding the behaviour of the Atlantic ocean circulation on multidecadal timescales has largely benefited from studies based on models forced at the surface by either synthetic or observed fluxes of heat, freshwater and momentum. The idea that the North Atlantic Oscillation (NAO, Hurrell, 1995) forcing is the main driver of Atlantic multidecadal variability was thus explored in a number of studies (e.g. Eden and Jung, 2001; Eden and Willebrand, 2001; Mecking et al, 2014). Although the processes and timescales involved in the oceanic

response may depend on both the exact nature of the forcings and the model configuration, the conclusion was reached that the NAO forcing is essential to the oceanic multidecadal variability and to reproduce part of the observed North Atlantic SST signal.

By contrast, when forced by fixed surface fluxes, idealized flat bottom ocean-only models have revealed their potential to generate multidecadal MOC oscillations (Colin de Verdière and Huck, 1999; Te Raa and Dijkstra, 2002). This intrinsic variability is associated with westward propagating Rossby waves, sustained through large-scale baroclinic instability. This mechanism has been shown to be robust to the coupling to a variety of idealized atmospheric models, like energy balance models (Fanning and Weaver, 1998; Huck et al, 2001) or zonally-averaged statistical-dynamical atmosphere (Arzel et al, 2007). This variability was also identified in realistic geometry ocean models, forced by fixed surface fluxes (Sévellec and Fedorov, 2013), or coupled to an atmospheric energy balance model (Arzel et al, 2012), but with a damped character due to a variety of processes. Introducing a 3D dynamical atmosphere, Buckley et al (2012) recently explored the multidecadal variability arising in two coupled model configurations with simplified flat bottom and bowl oceanic geometry. They highlighted the key role of unstable westward propagating Rossby waves in sustaining the oceanic variability. In flat bottom configuration, stochastic atmospheric variability was shown to be unnecessary to the existence of the variability. When the flat bottom approximation is relaxed, and idealized (Winton, 1997) or realistic (Sévellec and Fedorov, 2013) bottom topography added to the ocean model, the intrinsic oceanic variability may require an extra source of energy to be maintained. The atmosphere is a potential candidate to energize the oceanic variability, as shown in many studies

(e.g. Delworth and Greatbatch, 2000; Frankcombe and Dijkstra, 2009; Buckley et al, 2012).

Our study builds upon the work of Buckley et al (2012). The objective is to find out whether the intrinsic oceanic nature of the variability simulated by their flat bottom coupled model is modified when the horizontal resolution increases simultaneously in both the ocean and the atmosphere from 4° to 1°. Increasing the horizontal resolution has the potential to increase the intrinsic atmospheric variability and the atmospheric response to changes in ocean circulation (Hodson and Sutton, 2012), through an improved representation of transient eddy fluxes (see the review by Kushnir et al, 2002). Both processes can contribute to increase the role of the atmosphere in the low-frequency climate variability. Such resolutions remain beyond the scale required to resolve oceanic eddies, but mesoscale turbulence is though to have a minor impact on the existence of multidecadal oceanic variability (Penduff et al, 2011; Huck et al, 2015). The aim of this study is rather to shed light on the mechanisms of multidecadal variability in a North Atlantic-like ocean at low resolution. The Double Drake configuration of the MIT General Circulation Model (Ferreira et al, 2010; Marshall et al, 1997) used by Buckley et al (2012) is the starting point of our study. The focus is placed upon the influence of the atmospheric dynamics on the low frequency oceanic variability. Because the latter is affected by the presence of variable topography (Winton, 1997; Buckley et al, 2012), this study is carried out using only a flat bottom ocean configuration as a first step.

This paper is organized as follows. The coupled model is described in section 2, as well as the ocean and atmosphere climatological mean states of the three configurations with horizontal resolution of 4°, 2° and 1°. In section 3, we show

that the MOC is dominated by a 30-40 yr variability in all 3 set-ups, related to the propagation of large-scale Rossby waves. Density (dominated by temperature) anomalies propagate from east to west across the subpolar gyre, interacting with the MOC along the western boundary. At 1° resolution, the signal is less regular with more energy at high frequency. In section 4, the respective role of internal ocean dynamics and air-sea **interactions** in explaining the low-frequency oceanic variability is disentangled through the use of a linearized temperature variance equation, **and an ocean-only experiment**. In section 5, we finally summarize and discuss our results.

2 Description of the model and mean states

2.1 Numerical characteristics

We use the ocean-atmosphere-sea ice coupled MITgcm - Massachusetts Institute of Technology general circulation model (Marshall et al, 1997) - in the Double Drake configuration (Ferreira et al, 2010). The flat-bottom 3 km depth ocean has 15 vertical levels, with thickness increasing from 30 m at the surface to 400 m at the bottom, and two meridional barriers extended from the north pole to 34°S represented as physical walls of about 400 km width for the ocean. These continental barriers divide the ocean in a small, a large and an unblocked southern circumpolar basin, each of them aiming at crudely representing the Atlantic, the Indo-Pacific and the Southern ocean basin, respectively. The small basin is the site of a deep convection and deep overturning cell, referred to as the MOC in the following. The impacts of unresolved eddies are parametrized as an advective process (Gent and McWilliams, 1990) and an isopycnal diffusion (Redi, 1982) with

a transfer coefficient of 1200 m^2s^{-1} for both processes, in the range of observed values (Ollitrault and Colin de Verdière, 2002). Enhanced vertical mixing (100 m^2s^{-1}) of temperature and salinity applies whenever static instability occurs. The background vertical diffusivity is uniform and set to 3×10^{-5} m^2s^{-1}. These mixing coefficients are identical to those used by Ferreira et al (2010).

The atmospheric physics is based on the Simplified Parametrization, Primitive Equation Dynamics (SPEEDY, Molteni, 2003). It is a spectral model composed of 5 vertical levels. The parametrisations incorporated within the model are large-scale condensation, convection, diagnostic clouds, short-wave and long-wave radiation, surface fluxes and vertical diffusion.

Both oceanic and atmospheric models are integrated forward on the same cubed-sphere horizontal grid (Adcroft et al, 2004). This idealised coupled model is run in three configurations with increasing horizontal resolution. For the original set-up, each face of the cube has 24×24 grid points, leading to an horizontal resolution of about 4°. This set-up is referred to as cs24 hereafter (cs stands for Cubed-Sphere). This barely resolves the typical scale of synoptic atmospheric perturbations. The initial horizontal resolution of both ocean and atmosphere models is increased to cube faces divided in 48×48 and 96×96 horizontal grid points, resulting in horizontal resolution of about 2° and 1°, respectively (hereafter cs48 and cs96). The zonal extent of the land barriers is kept constant and roughly equal to 400 km. As the horizontal resolution of the dynamical core is increased, oceanic eddy lateral viscosity is reduced; the other physical parametrizations are unchanged. In particular vertical viscosity and turbulent diffusivities of oceanic eddies are kept constant. The main computational characteristics of the three configurations are summarized in table 1.

All three set-ups are initialised from the equilibrated oceanic state obtained by Ferreira et al (2010). Tracer fields (temperature T and salinity S) are interpolated to fit the new grids of cs48 and cs96. Atmospheric initial conditions for all 3 configurations are horizontally uniform and vertically stratified, and the model is initially free of ice. Under such initial conditions, both cs24 and cs48 quickly adjust, reaching equilibrium after less than 100 yr of integration, whereas cs96 requires more than 300 yr to reach equilibrium. During this 300 yr adjustment, the global mean oceanic temperature in cs96 decreases by about 0.6 K, and then slowly drifts by about 0.03 K/century. In both cs24 and cs48, the trend in temperature is smaller than 0.005 K/century. All set-ups are integrated forward in time for 600 yr. To analyse the longest time series and avoid adjustment period, we perform analyses on the last 400 yr. Mean state of cs48 and cs96 are first compared to the well documented mean state of cs24 (Ferreira et al, 2010; Buckley et al, 2012).

2.2 Atmospheric mean state

The zonal mean atmosphere is composed of two active baroclinic regions at mid-latitudes (Fig. 1), with westward jet streams reaching 40 m s^{-1} at 250 mb in cs24. Increasing the resolution has two main consequences for the atmosphere: eddy-driven jets shift poleward, and their amplitude weakens. The first consequence is common to many atmospheric models (Pope and Stratton, 2002; Arakelian and Codron, 2012). This poleward shift brings atmospheric model in better agreement with observations, revealing the necessity of a sufficiently high resolution to correctly represent a realistic climate. It is interesting to note that our idealized model reproduces a similar behaviour, highlighting its relatively high skills in simulat-

ing the mean state of the global climate. The weakening of the eddy-driven jets is associated with their widening, in agreement with Harnik and Chang (2004). As expected, the storm-tracks, computed as the standard deviation of daily Sea Level Pressure Anomaly (SLPA), strongly increase with the resolution (Pope and Stratton, 2002). The more vigorous storm-tracks are associated with an increased low frequency atmospheric variability (see section 4.1 for details).

For all set-ups, the poleward Atmospheric Heat Transport (AHT) is similar, peaking at about 4.5 PW (5-6 PW) at 40°N (40°S), in agreement with observations (Trenberth et al, 2001). The slight enhancement of AHT in the southern hemisphere is attributed to a more vigorous storm-track in this region (Ferreira et al, 2010), a north-south asymmetry observed at all resolutions. The mid-latitude AHT is almost entirely achieved by the eddy contribution at all resolutions, while the time mean circulation contributes only in the tropics.

2.3 Oceanic mean state

The realistic wind-stress forcing over the small basin (Fig. 1, bottom right panel) drives a barotropic circulation (Fig. 2, upper panels) composed of a weak tropical cyclonic gyre ($\sim$ 10 Sv, 1 Sv = 10^6 m^3s^{-1}), a subtropical anticyclonic gyre ($\sim$ 30 Sv) and a subpolar cyclonic gyre ($\sim$ 25 Sv). Following the poleward shift of the atmospheric jets, the position of the zero wind-stress curl line is displaced northward in the Northern Hemisphere with the increasing resolution. The intergyre position is displaced northward, and the subpolar cyclonic gyre in cs96 extends up to 70°N with a weak intensification along the western boundary. Due to weaker

polar easterlies in cs48 and cs96 (Fig. 1), the weak anticyclonic gyre ($\sim$ 2 Sv) present in cs24 north of 60°N disappears at higher resolution.

Increasing the horizontal resolution also strengthens the mean MOC maximum in the small basin from about 25 Sv in cs24 to about 30 Sv in cs96 (Fig. 2, bottom panels). Marsh et al (2009) observed a similar MOC strengthening in the OCCAM ocean model when the resolution is refined from 1/4° to 1/12°, but they mainly attributed this difference to the effect of resolved eddies. Here, the stronger MOC in cs96 is attributed to an increase of surface density resulting from increased heat losses and freshwater export over the northern small basin. North of 45°N, the zonally averaged oceanic heat loss over the small basin is about 20% (10 W m^{-2}) stronger in cs96 compared to cs24. In addition, Ferreira et al (2010) show that the small basin of the Double Drake model is characterized by a deep overturning cell due to the excess of net evaporation (evaporation minus precipitation, E-P) within this basin. This E-P excess is sensitive to horizontal resolution, with a significant enhancement north of 40°N, mainly due to increased evaporation within the small basin rather than reduced precipitation. This results in a more vigorous salinification of the small basin, and an enhanced MOC.

3 Oceanic multidecadal variability

We now focus our attention on the multidecadal oceanic variability in the small basin. At coarse resolution (cs24), Buckley et al (2012) have shown that the MOC undergoes a variability on multidecadal timescales. In their flat bottom configuration, the variability is described as an ocean-only mode damped by air-sea heat fluxes, with a red spectrum and a strong peak at a period of about 34 yr. In this

section, we investigate the robustness of the MOC multidecadal variability with respect to increased atmospheric and oceanic resolution, and the accompanying increase in atmospheric variability.

3.1 MOC variability

We use the MOC index defined by Buckley et al (2012) as the average of the small basin MOC in the box [8°-60°N, 460-1890 m depth] (black box in Fig. 2, bottom panels). Specifically, the yearly time series of the maximum MOC is computed at each latitude within the box, and then averaged across the range of latitude. To assess the coherence of this index, we compare it to 8 other time series related to the overturning (Table 2). Correlations between the initial index and the resulting time series are high ($r \geq 0.80$) except for the MOC at 63°N. These high correlations highlight the coherence of the MOC variability over the domain, and give confidence in the use of Buckley et al (2012) index at all three resolutions. This yearly index is computed over the last 400 yr of simulations (Fig. 3, left panel). It is used in the following as an indicator of the oceanic low-frequency variability. All analyses are performed with yearly outputs. However, results are weakly sensitive to the application of a 10-yr running mean. The MOC index presents a weak amplitude signal at multi-centennial timescales in cs96, with a weak positive (negative) trend between years 200-400 (400-600). The shortness of the model integration does not allow us to conclude whether this is an intrinsic oscillation or due to the longer adjustment of this set-up.

At all resolutions, the MOC undergoes a variability on multidecadal timescales, with an **increased amplitude** for cs48 and cs96 compared to cs24, and a noisier

variability for cs96. The power spectrum analysis of the yearly index reveals a dominant period of 32 yr for both cs24 and cs96, and 43 yr for cs48 (Fig. 3, right panel), consistent with time scales usually found in both models and observations (Frankcombe and Dijkstra, 2009; Frankcombe et al, 2010). The most important difference is the less regular MOC variations for cs96. We will show in section 4 that this difference mainly results from a stronger impact of atmospheric variability on the ocean circulation.

The western boundary has been shown to be a key region to monitor the MOC variability (Hirschi and Marotzke, 2007; Tulloch and Marshall, 2012; Buckley et al, 2012). Those studies relate the MOC variability to the east-west boundary density difference through the thermal wind relationship (see Appendix 2). Following their work, we reconstruct the variability of the MOC index by computing the zonally integrated geostrophic meridional velocity resulting from the difference between density anomalies along the eastern and the western boundary (Eq. (4) in Appendix 2). The resulting meridional velocities are vertically integrated to obtain the reconstructed MOC anomaly ψ^*_ρ (Eq. (5), Fig. 4 red curves). The MOC index computed from ψ^*_ρ is compared to the model MOC index by computing the skill S between these two time series (Eq. (8)). The skill for the reconstructed MOC index is 0.78 (0.93, 0.94) for cs24 (cs48, cs96, respectively). These good skills highlight the dominant contribution of the geostrophic shear for the MOC variations (the Ekman shear plays a minor role and the contribution of the barotropic mode is strictly zero due to flat bottom).

We can go a step further in the approximation by considering only temperature anomalies along the western boundary in Eq. (7) ($\psi^*_{T_w}$, Fig. 4, blue curves). The matching between the model and $\psi^*_{T_w}$ MOC indices is striking, revealing

the key role of the western boundary temperature anomalies in explaining MOC variations. In cs96 however, both indices present a trend (black and blue dashed lines on Fig. 4, right panel), probably due to the longer adjustment of this set-up (see section 2.1). To solely keep the decadal variations in computing the skill between the reconstructed MOC index and the model MOC index, these trends have been preliminary removed. By only considering temperature anomalies along the western boundary, the skill reduces to $S = 0.15$ (0.46, 0.58) for cs24 (cs48, cs96, respectively). These low skills mainly reflect the lag of few years between the model and $\psi^*_{T_w}$ MOC indices, **(Fig. 4, black and blue curves respectively). However the 2 time series are relatively well correlated with** $r = 0.66$ **(0.82, 0.78) for cs24 (cs48, cs96, respectively). When the lag is removed and both time series are in phase, the correlation reaches** $r = 0.79$ **(0.90, 0.84).**

Analysis of $\psi^*_{T_w}$ **demonstrates that the MOC variability in all set-ups is mainly geostrophic, driven by temperature anomalies along the western boundary. These anomalies can be tracked along the western boundary to understand MOC variability (Fig. 5).** Negative temperature anomalies on the western boundary, with a subsurface intensification between 40°-60°N, are associated with positive MOC anomalies. They strike the western boundary few years before a MOC minimum, travel southward and downward following the mean isotherms, and lead to MOC anomalies further south (not shown).

3.2 Associated temperature anomalies

The small basin is characterized by large scale, depth coherent, temperature anomalies that covary with the MOC index. To illustrate this, yearly potential temper-

ature anomalies averaged over the 1000 m upper ocean (referred to as T1000 further) associated with one standard deviation of the MOC index with different phase lags are shown on Fig. 6 (see caption for details). Prior a MOC maximum, positive T1000 anomalies appear and grow along the eastern boundary, and spread almost all over the subpolar gyre after a MOC maximum. Negative anomalies experience the same dynamics around a minimum of MOC. The horizontal signature of large-scale T1000 anomalies is harder to track in cs96, with more complex patterns (Fig. 6, bottom row panels). We still observe negative (positive) T1000 anomalies within the subpolar gyre prior (after) a MOC maximum, but the region of growth along the eastern boundary observed at coarser resolution is no longer significant.

Large-scale baroclinic instability has been proposed for sustaining these perturbations (Colin de Verdière and Huck, 1999). This mechanism is principally identified through the vertical structure of temperature anomalies, and the associated meridional eddy heat fluxes (the latter will be discussed in section 4.2.1). The vertical structure of temperature anomalies is computed within the region of highest standard deviation of T1000, between 60°-70°N, near the eastern boundary. Temperature anomalies are intensified at sub-surface, with a maximum at 265 m depth for cs24 and at 540 m depth for both cs48 and cs96, highlighting their surface damping by turbulent atmospheric fluxes. They exhibit a vertical tilt, with sub-surface anomalies leading deep anomalies with a quarter phase lag, in agreement with classical theory (Colin de Verdière and Huck, 1999; Sévellec and Huck, 2015).

To illustrate the westward propagation across the basin, longitude-time (Hovmöller) diagrams have been computed at various latitudes. It appears that 60°N, 65°N and 70°N are the most relevant ones to capture the propagating signal for cs24, cs48

and cs96, respectively. It is interesting to note that these specific latitudes also roughly correspond to the zero-wind stress curl line associated with large scale wind distribution described in section 2.2. Hovmöller diagrams computed at these latitudes (Fig. 7), show a westward propagation of temperature anomalies, with an estimated phase velocity of about 0.40 cm s^{-1} for all experiments. They propagate slower in the eastern half of the small basin (0.36, 0.26 and 0.21 cm s^{-1} for cs24, cs48 and cs96, respectively) than in the western half (0.83, 0.70 and 0.74 cm s^{-1}), as estimated from the slope of the white lines in Fig. 7. The phase speed of baroclinic modes computed from the mean stratification in the quasigeostrophic approximation (Huck et al, 2001, section 2c) does not explain such a speed-up in the western region. Taking into account the advection of anomalies by the mean barotropic flow (Doppler shift) qualitatively explains the observed acceleration westward, but underestimates the phase velocity. Incorporating the vertical shear of the mean flow within the baroclinic mode computation clearly improves the results: A detailed analysis is underway and will be reported in a dedicated study.

We now look at SST signature associated with the MOC variability because of its critical role for ocean-atmosphere interactions. Fig. 8 illustrates SST anomalies associated with one standard deviation of the MOC index (non-significant regressions are grey shaded). In all set-ups, these SST anomalies account for more than 50% of the total SST variability, but their global structures are very different between cs48/cs96 and cs24. For cs24, it is closely related to the propagation of large-scale temperature anomalies described in section 3.2. They emanate near the eastern boundary and propagate westward around 60°N. In cs48, positive anomalies are observed in two different regions: one along the eastern boundary, north of 60°N, and one along the western boundary in the subpolar gyre. The first one

is the surface signature of Rossby waves, propagating from east to west, while the second seems to be stationary. As the first one propagates toward the west, it slowly merges with the second one.

In both cs48 and cs96, SST are dominated by a widespread positive anomaly that covers the entire subpolar gyre, as observed in many other models (Danabasoglu, 2008; Zhang, 2010; Tulloch and Marshall, 2012) and observations (Knight et al, 2005). Such a pattern is usually referred to as the Atlantic Multidecadal Oscillation (AMO) (Kerr, 2000; Enfield et al, 2001). The warming of the subpolar gyre induced by a strengthening of the MOC is usually attributed to a more vigorous Oceanic Heat Transport (OHT) (Knight et al, 2005; Zhang, 2008). In our model, OHT anomalies associated with one standard deviation of the MOC index peak at about 0.03 PW (0.08, 0.06) at the subtropical-subpolar intergyre position for cs24 (cs48, cs96, respectively). They account for more than 65% of the OHT variability at this latitude. **While these OHT anomalies are significantly larger in cs48 and cs96, the regression coefficients between OHT and the MOC index are similar for all set-ups, such that larger OHT anomalies observed in cs48 and cs96 mainly result from a stronger MOC variability. They are mainly driven by the zonally integrated circulation (the MOC) in the subtropical gyre and by the gyre circulation (computed as the residual) in the subpolar gyre, and the partition between MOC and gyre OHT anomalies is relatively similar for all set-ups.** Through OHT anomalies, larger (positive) MOC anomalies in cs48 and cs96 induce positive SST anomalies within the subpolar gyre, as observed in Fig. 8. This advective process (OHT) conceals the surface signature of large scale baroclinic Rossby waves in cs48 and cs96. By contrast, the weaker OHT anomalies in cs24 induce weaker SST anomalies, allowing a much

clearer surface signature of such waves. The main idea to keep in mind is that SST anomalies that covary with the MOC (Fig. 8) present a different signature between cs24 and cs48/cs96, that can result in/from different air-sea interactions. This is what we aim to analyse in the following.

4 Role of atmospheric forcing and ocean dynamics

We have shown that the MOC undergoes a similar variability in all set-ups, related to the propagation of large-scale baroclinic Rossby waves. At increasing horizontal resolution, the SST variability is different between cs24 and cs48/cs96, especially along the western boundary. This may have important implications for air-sea interactions. In this section, we aim to disentangled the respective role of internal ocean dynamics and air-sea interactions in explaining the low-frequency oceanic variability.

4.1 Atmospheric variability

To help the discussion on the role of the atmospheric forcing for the low-frequency oceanic variability, we first focus on the internal atmospheric variability. **It is traditionally diagnosed with the use of the first EOF of Sea Level Pressure Anomaly (SLPA) in the North Atlantic or the northern hemisphere, and referred to as the North Atlantic Oscillation (NAO, Hurrell, 1995) or the Northern Annular-Mode (NAM, Thompson and Wallace, 2001). Both processes result from internal atmospheric dynamics (Vallis et al, 2004, and references therein). The zonal asymmetry of the NAM/NAO is principally induced by land-sea contrasts (Thompson and Wallace, 1998), and the ab-**

sence of realistic continents in our model favours the emergence of the NAM rather than the NAO. Because both NAM and NAO indices are highly correlated (Deser, 2000), the NAM is used in the following in a similar manner as realistic model studies use the NAO.

In our model, the first EOF of the yearly SLPA explains about 60% of the variance in all set-ups, with a slight enhancement at increasing resolution (Fig. 9). Its spatial structure is zonally uniform, with anomalies of opposite sign north/south of 60°N. Because this pattern resembles the NAM, it is referred to as such hereafter. The amplitude of the atmospheric variability associated with the first EOF/PC (i.e. the NAM index) is computed with the absolute maximum of the spatial EOF1 pattern obtained with a projection onto the standardized PC1 (Table 1). We observe a strong enhancement of the intrinsic atmospheric variability with increasing horizontal resolution, with a NAM amplitude that almost doubles from cs24 to cs96. The NAM variability is increased for all time scales, revealing a white spectrum of the atmosphere variability at low frequencies.

To estimate the impact of the enhanced atmospheric variability on the oceanic low frequency oscillation, we compute the correlation between the yearly SLPA in the northern hemisphere and the yearly MOC index. Using a statistical significance test based on a Monte Carlo approach (see Appendix 1), the most significant correlations are found when the SLPA leads the MOC by 2 yr in all set-ups (Fig. 10). At this lag, the correlation is significant only near the small basin northern corner and in the tropics for cs48, whereas for cs24 **almost no** significant correlations are obtained. This reveals the weak interaction between the oceanic and the atmospheric variability at those resolutions. By contrast, a much more important

fraction of the SLPA is significantly correlated to the MOC variability in cs96, with negative (positive) correlations northward (southward) of 60°N. This pattern strongly resembles the NAM described above. By increasing the horizontal resolution up to 1°, the intrinsic atmospheric variability is enhanced and becomes significantly correlated to the MOC variability in cs96, with the NAM that leads by 2 years the MOC variability. This feature is common to many other numerical studies (Eden and Jung, 2001; Deshayes and Frankignoul, 2008; Gastineau and Frankignoul, 2012), with a positive phase of the NAO that leads a maximum of MOC by few years. They describe the MOC variability in the North Atlantic as an oceanic response to stochastic atmospheric forcing. More recently, McCarthy et al (2015) have shown than the observed NAO leads by 2-3 years their sea-level index, a proxy for the ocean circulation at the intergyre position. Regarding these results, we therefore ask the following question: Does the oceanic mode of variability reproduced in our idealized model switch from an intrinsic oceanic mode at coarse resolution (cs24), as shown by Buckley et al (2012), to an oceanic mode forced by the atmosphere at higher resolution (cs96)? This issue is further investigated in the following.

4.2 Creation of temperature variance

The respective role of internal ocean dynamics and air-sea interactions in explaining the low-frequency oceanic variability is disentangled through the use of the linearized temperature variance equation (Colin de Verdière and Huck, 1999; Te Raa and Dijkstra, 2002; Arzel et al, 2006):

$$\overline{\partial_t \epsilon} = -\overline{\mathbf{u}}.\nabla\overline{\epsilon} - \overline{\mathbf{u}'T'}.\nabla\overline{T} + \overline{T'Q'} + \overline{T'D'} \quad (1)$$

where $\epsilon = T'^2/2$ is the temperature variance, the overbar denotes a time average over several oscillation periods and the prime the deviation from the time average (i.e. yearly anomalies), $\mathbf{u}$ and T the 3D velocity and temperature field, Q ocean-atmosphere heat fluxes (positive downward) and D the oceanic diffusion. The cubic eddy correlation terms are neglected because the perturbations observed remain small compared to the mean state. The first term of the rhs represents the transport of temperature variance by the mean flow $\overline{\mathbf{u}}$. It simply redistributes the variance in the domain and cannot be a source of energy since it is zero globally. The second term is a source of variability if the eddy temperature fluxes $\overline{\mathbf{u}'T'}$ are oriented down the mean temperature gradient $\nabla\overline{T}$. This term has been pinpointed as the energy source for the variability under constant surface buoyancy fluxes in the experiments of Colin de Verdière and Huck (1999) and Te Raa and Dijkstra (2002). Under mixed surface boundary conditions by contrast, Arzel et al (2006) identified a convective-surface heat flux feedback where the third term $\overline{T'Q'}$ is the driver of multidecadal variability (this term is discussed in section 4.2.2). The last term ($\overline{T'D'}$) represents a sink of energy due to diffusive and convective processes. Therefore, determining which of the second or third terms (i.e. the only possible sources of energy) in the rhs of (1) dominates the balance may help to elucidate the physical mechanisms governing the variability.

4.2.1 Internal oceanic dynamics

The role of oceanic dynamics is diagnosed following the work of Colin de Verdière and Huck (1999). They show that in order for an instability to grow against mixing and atmospheric damping, oceanic eddy temperature fluxes have to be oriented down the mean temperature gradient, i.e. $-\overline{\mathbf{u}'T'}.\nabla\overline{T} > 0$ (see Eq. (1)). When

positive, this term represents a transfer of mean potential energy to eddy kinetic and potential energy, which tends to relax mean temperature gradients. This term indicates the regions of growth of the perturbations. Here, this term is computed using the yearly temperature and velocities fields, and results are averaged over the upper 1000 m (Fig. 11).

For cs24, the region where the magnitude of $-\overline{\mathbf{u}'T'}.\nabla\overline{T}$ is the largest is located near the eastern boundary, around 60°N, in agreement with results of Buckley et al (2012). For cs48 and cs96, this region shifts near the subpolar gyre western boundary, between 50°-60°N. Averaged over the small basin, $-\overline{\mathbf{u}'T'}.\nabla\overline{T}$ is positive in all set-ups, and is mainly driven by positive meridional eddy fluxes ($\overline{v'T'}$), oriented down the mean meridional temperature gradient ($\partial_y\overline{T} < 0$). The zonal and vertical contributions play a secondary role. Hence the growth of temperature variance through large-scale baroclinic instability mostly takes place in the vicinity of the western boundary for cs48 and cs96, but mostly along the eastern boundary for cs24.

4.2.2 Air-sea heat fluxes

At multidecadal timescales, the transfer of atmospheric variability into the ocean is usually attributed to heat fluxes exchange (Timmermann et al, 1998; Delworth and Greatbatch, 2000). These fluxes have also been pinpointed as a source of variability for the oceanic low frequency variability under mixed surface boundary conditions (Arzel et al, 2006). Such a transfer is diagnosed here by computing the correlation between the surface heat flux anomalies (Q') and the SST anomalies (T'), i.e. the third term of the rhs of (1). Both heat fluxes and SST anomalies are filtered with a 10 yr running mean, referred to as the long-term signal hereafter. Here, Q' is

positive downward for a heat flux from atmosphere to ocean: $Q' \propto (T'_a - T')$, with T'_a and T' the atmospheric and oceanic temperature at the interface, respectively. Lets consider the case of a negative heat flux anomaly ($Q' < 0$) with all other fluxes at rest. It can either mean that the ocean is warmer than normal ($T' > 0$ and $T'_a = 0$) or that the atmosphere is colder than normal ($T'_a < 0$ and $T' = 0$). In the case of $T' > 0$, the negative correlation $T'Q' < 0$ results from oceanic dynamics, and (1) shows that air-sea forcing is damping the low frequency oceanic variability. On the other hand, if $T'_a < 0$, the atmosphere will extract heat from the ocean, inducing $T' < 0$ and hence a positive correlation $T'Q' > 0$. In the framework of (1), the atmospheric variability will induce an oceanic variability through heat fluxes. The same conclusions can be reached by considering the case of positive heat fluxes anomalies. On long time cales, the small basin north of 30°N is dominated by negative correlations (Fig. 12, top row panels), indicating that the ocean-atmosphere heat fluxes are driven by the oceanic dynamics. The third term of (1) is then a sink for the oceanic low-frequency variability, and SST anomalies observed in Fig. 8 are damped by atmospheric heat fluxes. Between 10°-30°N, we observe a band of positive correlation ($T'Q' > 0$). However, on these timescales, tropical SST (Fig. 8) are not significantly correlated to the MOC variability. Such a correlation between SST and heat fluxes short-term variability may then not have a significant impact on the intrinsic oceanic low frequency MOC variability.

Using observational data, Gulev et al (2013) have confirmed the Bjerknes (1964) assumption for the North Atlantic sector: Q' is driven by ocean dynamics on long-term (multidecadal timescales), but by the atmospheric dynamics on short-term (interannual to decadal timescales). To investigate this issue in our model, we compute now the short-term signal by taking the deviation from the long-term

signal, i.e. the 10-yr-smoothed temperature and heat fluxes anomalies. The 10-yr smoothing window appears to be an ideal time filtering to clearly separate the oceanic and atmospheric role in the heat fluxes variability (Gulev et al, 2013). On short-term (Fig. 12, bottom row panels), the correlation is positive almost all over the small basin. At those timescales, ocean-atmosphere heat fluxes are mainly driven by the atmosphere, consistent with the stochastic forcing of the ocean in the Frankignoul and Hasselmann (1977)'s paradigm, and the results of Gulev et al (2013). However, a negative correlation is observed along the western boundary of the subpolar gyre, and spreads over a wider region as the resolution increases. In this region, the short-term heat fluxes variability is driven by the ocean dynamics rather than the atmosphere.

It has been proposed that OHT controls air-sea heat fluxes at interannual time scales in the Western North Atlantic, mainly through geostrophic advection (Dong et al, 2007; Buckley et al, 2015). This supports the idea that SST anomalies along the western boundary of the subpolar gyre observed in cs48 and cs96 (Fig. 8) result from OHT convergence at this location. The atmosphere damps the SST anomalies, resulting in a negative correlation $T'Q' < 0$. This correlation gets stronger with increasing resolution, but not the SST variability as described at the end of section 3.2. Processes that are resolution dependent may also explain this increase in a negative correlation. Recent studies (Minobe et al, 2008; Skyllingstad et al, 2007) show that sharp SST fronts typical of western boundary regions tend to destabilize the Marine Atmospheric Boundary Layer, resulting in atmospheric dynamics that are directly driven by the underlying ocean. In our model, the sharpening of SST gradients along the western boundary resulting from the increased oceanic resolution might induce a stronger atmospheric response, explaining the increased

correlation $T'Q'$ at higher resolution. This atmospheric response could ultimately feedback into the ocean. However, such barely resolved processes are out of the scope of this paper.

4.3 Ocean only experiments

To further investigate the influence of air-sea interactions for the low frequency oceanic variability in cs96, we have run an ocean-only experiment. The ocean is forced at the surface by 5-day climatological fresh water and momentum fluxes. The forcing in temperature is composed of a 5-days climatological flux term, and a restoring toward the 5-day climatological SST, with a time scale of about 72 days (coupling coefficient $\alpha = 20\ Wm^{-2}K^{-1}$ (Frankignoul et al, 1998)). All terms are extracted from the coupled model, which will be referred to as CPL hereafter. Oceanic initial conditions are the oceanic state of CPL after 400 yr of integration. This ocean-only experiment (referred to as CLIM-FLX hereafter) is integrated for 200 yr. A similar experiment has been conducted by Buckley et al (2012) to show the intrinsic nature of the oceanic variability in cs24. Their ocean-only experiment reproduced in close agreement the low-frequency MOC variability of their flat bottom coupled configuration, demonstrating that the stochastic atmospheric forcing is not essential for the oceanic variability. Such a conclusion remains valid for cs96. The CLIM-FLX experiment reproduces relatively well the MOC variability of CPL, with a strong peak of variability at 43 yr (Fig. 13). As revealed by time series and power spectrum, the regularity of the MOC variations is strongly increased in CLIM-FLX, with less interannual variability, but almost the same energy at multidecadal time scales. Within the subpolar gyre, the propagation of

large scale baroclinic Rossby waves has a more regular signature (Fig. 7, bottom right panel), with an averaged phase velocity from eastern to western boundary of about 0.33 cm s^{-1}, just as in CPL. Consequently, air-sea interactions in CPL clearly disrupt the propagation of large scale baroclinic Rossby waves, perturbing the regularity of the MOC variability.

5 Summary and discussion

In this paper, we have investigated the role of air-sea interactions in the multidecadal variability of the Meridional Overturning Circulation (MOC). We used both fully coupled and ocean only GCM runs with an idealized flat-bottom aquaplanet geometry and two meridional boundaries. This Double Drake configuration reproduces some aspects of the present climate (Ferreira et al, 2010). Three set-ups, with horizontal resolution of about 4°, 2° and 1° (cs24, cs48 and cs96, respectively) in both the ocean and the atmosphere, are compared. Cs48 is run in a coupled configuration only, while both cs24 and cs96 are run in coupled and ocean-only configurations. By increasing the horizontal resolution in both the ocean and atmosphere models, we have increased the intrinsic atmospheric variability, which is almost doubling from cs24 to cs96. In contrast, mesoscale eddies are still not resolved in the ocean. The main results can be summarized as follow:

1. In all coupled configurations, the MOC exhibits an intrinsic oceanic mode of variability on time scales of 30-40 yr. It is related to large-scale oceanic baroclinic Rossby waves that originate and propagate along the climatological mean zero-wind stress curl line, corresponding to the northern extent of the subpolar gyre.

2. Using a temperature variance budget, the origin of the multidecadal variability is identified as an internal oceanic mode sustained through the growth of large-scale baroclinic Rossby waves, while air-sea interactions have a damping influence. The growth of baroclinic Rossby waves mostly takes place in the vicinity of the western boundary for cs48 and cs96, but mostly along the eastern boundary for cs24.
3. In concert with increased intrinsic atmospheric variability, we found in cs96 a statistically significant correlation between the Northern Annular-Mode (NAM) and the MOC variability when the NAM leads by 2 yr.
4. The effect of atmospheric coupling tends to perturb the propagation of oceanic large-scale baroclinic Rossby waves across the basin in cs96, destabilizing the regularity of the oceanic oscillations. In this set-up, the MOC variability is an intrinsic oceanic mode, despite significant lag correlations between the NAM and the MOC.

The robustness of the multidecadal MOC variability reproduced in all flat bottom coupled configurations presented in this study complements the ocean-only experiments forced by fixed surface fluxes (Colin de Verdière and Huck, 1999), coupled to an atmospheric energy balance model (Huck et al, 2001; Fanning and Weaver, 1998), or coupled to a zonally averaged atmospheric model (Arzel et al, 2007). By coupling the ocean to a dynamical atmospheric component, we have climbed a further step in the realism of ocean-atmosphere interactions, and yet the same mechanism appears to be at work.

The development in cs96 of atmospheric variability that is significantly correlated to the MOC variability highlights the importance of a sufficiently high

horizontal resolution to reproduce ocean-atmosphere interactions at decadal time scales. A similar conclusion has been reached by Hodson and Sutton (2012) using the realistic HadGEM2.1 coupled model run at two different horizontal resolutions (1° and $\frac{1}{3}^\circ$): The atmospheric pattern correlated to the low-frequency oceanic variability is much more significant at higher resolution. Such a correlation is a robust feature of many high resolution realistic models (Eden and Willebrand, 2001; Deshayes and Frankignoul, 2008; Gastineau and Frankignoul, 2012), with a positive phase of the NAO that occurs few years prior a MOC maximum. These studies describe the MOC variability in the Atlantic as an oceanic response to the atmospheric forcing, through a fast oceanic barotropic response to NAO-induced surface wind stress. A similar connection is drawn by Sun et al (2015) in their delayed oscillator model to explain the NAO low-frequency variability, but involves a time delay between the NAO and the Atlantic MOC of about 15 yr. Here, conducting an ocean-only simulation forced by constant fluxes for cs96 (denoted as CLIM-FLX), we prove that a significant lag correlation between SLPA and MOC does not imply that the oceanic low frequency variability is forced by the atmosphere. These results contrast with those of Delworth and Greatbatch (2000) who found in the GFDL coupled model that the 40-80 yr MOC variability mainly results from ocean-atmosphere heat fluxes driven by the intrinsic atmospheric low-frequency variability. Here, we have shown that at multidecadal time scales, ocean-atmosphere heat fluxes in the northern Atlantic basin are a consequence rather than a cause of internally driven ocean variability. Air-sea interactions are not crucial for the existence of the low frequency mode, but impact its expression.

These results may be discussed in two ways. First, even if the correlation between the atmospheric and oceanic low frequency variability is strongly enhanced

at increasing resolution, the atmospheric response in the Double Drake model might remain too weak to efficiently influence the ocean mode. By increasing the horizontal resolution up to 1°, we have doubled the intrinsic atmospheric variability, but this resolution remains beyond the one necessary to significantly capture, for instance, the impact of oceanic fronts onto the atmosphere, maybe around 50 km (Minobe et al, 2008). Those small scale ocean-atmosphere interactions might be of primary importance to reproduce an active atmosphere dynamics setting the oceanic low-frequency variability. However, studies that describe the multi-decadal climate variability as a coupled mode or as an oceanic mode forced by atmospheric variability do not claim the necessity of such small scale processes. They usually involve large scale ocean-atmosphere interactions. For instance, Timmermann et al (1998) described a coupled mode of variability in the 4° horizontal resolution ECHAM-3/LSG coupled model, such that large scale ocean atmosphere interactions between extratropical SST and atmospheric dynamics can be sufficient to generate a coupled mode of variability.

Secondly, the mechanisms proposed in high resolution climate model studies are rarely related to the propagation of Rossby waves. Indeed, Winton (1997) show that the ocean bathymetry may damp the intrinsic oceanic variability. In the same Double Drake model (the one used in this study), Buckley et al (2012) have shown that the introduction of an idealized bowl bathymetry switches the type of mode of variability from an ocean-only mode damped by atmospheric fluxes (with flat-bottom), to a damped oceanic mode stochastically excited by atmospheric fluxes (with bowl bathymetry). The impact of the bottom topography on the MOC variability is principally attributed to the disruptive effect of the topography on the propagation of large-scale baroclinic Rossby waves. These results cast some doubt

on the **existence of these waves** in realistic climate models or in the real ocean. However, using observational data, Frankcombe et al (2008) observed the signature of large-scale SST and Sea Surface Height anomalies, propagating westward across the North Atlantic ocean. In addition, Sévellec and Fedorov (2013) show that, in a 2° global configuration of the OPA (Océan PArallélisé) model with realistic topography, the least damped mode of variability of the tangent adjoint linear model remains a potential candidate to explain the MOC multidecadal variability (Ortega et al, 2015). This mode is characterized by large-scale temperature anomalies that propagate westward across the subpolar gyre, associated with long baroclinic Rossby waves (Sévellec and Huck, 2015). It will be important to see how a realistic oceanic topography might influence the oceanic mechanism found in this study.

Acknowledgements We acknowledge the help from John Marshall, David Ferreira and Martha Buckley at MIT for providing the Double Drake model used in this study as well as post-processing routines, and for assistance in understanding the MITgcm environment. We thank the MIT EAPS group for hosting Q. Jamet when setting up cs48 and cs96 configurations. We also thank Guillaume Gastineau at LOCEAN/IPSL for providing routines to compute the statistical significance test, as well as for constructive discussions. Computational resources were provided by the Pôle de Calcul Intensif pour la Mer at Ifremer, Brest, France, and through a GENCI allocation attributed to O. Arzel.

Appendix 1: Statistical significance test using Monte Carlo approach

The significance of a regression or a correlation is computed with a Monte Carlo approach. It consists in comparing the regression/correlation being tested to the regression/correlation of a randomly scrambled ensemble. Say we want to estimate the significance of the regression of a field $\lambda(x, y, t)$ onto a time series (usually the Meridional Overturning Circulation) $MOC(t)$, t being the time in yr, x and y the zonal and meridional coordinates. We first compute the initial regression maps, denoted as $reg_{\text{init}}(x, y)$.

At each grid point (x_i, y_j), the time series $\lambda(x_i, y_j, t)$ is randomly permuted by blocks of 3 yr to reduce the influence of serial autocorrelation. The regression $reg_{k1}(x_i, y_j)$ between the resulting time series $\lambda_{\text{permut}}(x_i, y_j, t)$ and $MOC(t)$ is performed. This analysis is repeated N times, resulting in N different randomly permuted regression $reg_k(x_i, y_j)$, $k = (k_1, k_2, ..., k_N)$. The estimated significance level is the percentage of randomized regression that exceeds the regression being tested:

$$signif(x_i, y_j) = \frac{\sum_{k=1}^{N} reg_k(x_i, y_j) > reg_{init}(x_i, y_j)}{N} \tag{2}$$

A smaller significance level indicates the presence of stronger evidence against the null hypothesis. In this paper, we fix the threshold of significance to 5%. This statistical significant test is applied for all regression / correlation analyses performed.

Appendix 2: MOC anomalies reconstruction from the difference between density/temperature anomalies along the western and eastern boundaries

Hirschi and Marotzke (2007) show that the MOC variability can be reconstructed through the thermal wind relationship by considering boundary density anomalies. This reconstruction does include neither the Ekman shear mode nor the barotropic velocities. In flat bottom configuration, the latter is strictly zero, which facilitates the reconstruction in our case.

The thermal wind relationship

$$f\partial_z v = -\frac{g}{\rho_0}\partial_x \rho, \tag{3}$$

is used as the starting point, with f the Coriolis parameter, v the meridional velocity, g the earth's acceleration, ρ the density and ρ_0 its reference value. Integrating zonally and vertically the perturbation part of Eq. (3), with the condition $v'(z=-H)=0$, leads to

$$\overline{v'(z')}^x = \int_{x_w}^{x_e} v' dx = -\frac{g}{\rho_0 f}\int_{-H}^{z'} (\rho'_e - \rho'_w) dz \tag{4}$$

We reconstruct a geostrophic MOC anomaly ψ^*_ρ as the vertical integration of $\overline{v'(z')}^x$:

$$\psi^*_\rho(z') = \int_{-H}^{z'} \left[\overline{v'}^x - \frac{1}{H}\int_{-H}^{0} \overline{v'}^x dz\right] dz, \tag{5}$$

where $\frac{1}{H}\int_{-H}^{0} \overline{v'}^x dz$ has been substracted in order to ensure that $\psi^*_\rho(z'=0) = \psi^*_\rho(z'=-H) = 0$.

We can go a step further in the approximation by only considering the temperature contribution. The thermal wind relationship reduces to

$$f\partial_z v = g\alpha\partial_x T \tag{6}$$

with $\alpha = 2.10^{-4}\ K^{-1}$, the thermal expansion coefficient. Performing a similar integration, we obtain a reconstructed MOC anomaly ψ^*_T computed with a zonally integrated meridional velocities anomalies of the form

$$\overline{v'(z')}^x = \int_{x_w}^{x_e} v' dx = \frac{g\alpha}{f}\int_{-H}^{z'} (T'_e - T'_w) dz, \tag{7}$$

with T'_e and T'_w the temperature anomalies along the eastern and western boundaries, respectively. We can also compute the contribution from the western boundary temperature anomalies only, $\psi^*_{T_w}$.

703 Note that this method misses one half grid point at the eastern and western boundaries.
704 Both temperature and density anomalies that are used to reconstruct the MOC variability are
705 located at the centre of the cell, rather than right along boundaries. This error is dependent
706 on the horizontal resolution, and partially explains why the reconstructions are more accurate
707 at higher resolution.

The geostrophic MOC indices are computed in the same way as for the model. The skill for the geostrophic MOC index (I_{ψ^*}) accounting for the variance of the model MOC index (I_{MOC}) is defined as

$$S = 1 - \frac{< (I_{MOC} - I_{\psi^*})^2 >}{< (I_{MOC})^2 >} \tag{8}$$

708 with $< . >$ a time average operator. $S \in [-\infty; 1]$, and $S \to 1$ indicates that the geostrophic
709 MOC index and the model MOC index vary in phase and are of the same magnitude. Negative
710 values denote a low or negative correlation and/or that the amplitude of I_{ψ^*} is larger than
711 I_{MOC}.

References

Adcroft A, Campin JM, Hill C, Marshall J (2004) Implementation of an atmosphere-ocean general circulation model on the expanded spherical cube. Mon Wea Rev 132(12):2845–2863

Arakelian A, Codron F (2012) Southern Hemisphere Jet Variability in the IPSL GCM at Varying Resolutions. J Atmos Sci 69:3788–3799

Arzel O, Huck T, Colin de Verdière A (2006) The Different Nature of the Interdecadal Variability of the Thermohaline Circulation under Mixed and Flux Boundary Conditions. J Phys Oceanogr 36:1703–1718

Arzel O, Colin de Verdière A, Huck T (2007) On the origin of interdecadal oscillations in a coupled ocean–atmosphere model. Tellus 59A:367–383

Arzel O, England MH, Colin de Verdière A, Huck T (2012) Abrupt millennial variability and interdecadal-interstadial oscillations in a global coupled model: sensitivity to the background climate state. Clim Dyn 39:259–275

Bjerknes J (1964) Atlantic air-sea interaction. Advances in geophysics 10(1):1–82

Buckley MW, Ferreira D, Campin JM, Marshall J, Tulloch R (2012) On the relationship between decadal buoyancy anomalies and variability of the Atlantic meridional overturning circulation. J Clim 25(23):8009–8030

Buckley MW, Ponte RM, Forget G, Heimbach P (2015) Determining the origins of advective heat transport convergence variability in the North Atlantic. J Clim (2015)

Chylek P, Folland CK, Dijkstra HA, Lesins G, Dubey MK (2011) Ice-core data evidence for a prominent near 20 year time-scale of the Atlantic Multidecadal Oscillation. Geophys Res Lett 38(L13704)

Colin de Verdière A, Huck T (1999) Baroclinic instability: An oceanic wavemaker for interdecadal variability. J Phys Oceanogr 29(5):893–910

Danabasoglu G (2008) On multidecadal variability of the Atlantic meridional overturning circulation in the community climate system model version 3. J Clim 21(21):5524–5544

Delworth T, Manabe S, Stouffer R (1993) Interdecadal variations of the thermohaline circulation in a coupled ocean-atmosphere model. J Clim 6(11):1993–2011

741 Delworth TL, Greatbatch RJ (2000) Multidecadal thermohaline circulation variability driven
742 by atmospheric surface flux forcing. J Clim 13(9):1481–1495
743 Delworth TL, Zhang R, Mann ME (2007) Decadal to centennial variability of the Atlantic from
744 observations and models. Geophysical Monograph 173:131–148, ocean circulation: Mecha-
745 nisms and Impacts
746 Deser C (2000) On the teleconnectivity of the Arctic Oscillation. Geophys Res Lett 27(6):779–
747 782
748 Deshayes J, Frankignoul C (2008) Simulated variability of the circulation in the North Atlantic
749 from 1953 to 2003. J Clim 21(19):4919–4933
750 Dong S, Hautala SL, Kelly KA (2007) Interannual variations in upper-ocean heat content and
751 heat transport convergence in the western North Atlantic. J Phys Oceanogr 37(11):2682–
752 2697
753 Eden C, Jung T (2001) North Atlantic interdecadal variability: Oceanic response to the North
754 Atlantic Oscillation (1865-1997). J Clim 14:676–691
755 Eden C, Willebrand J (2001) Mechanism of interannual to decadal variability of the north
756 atlantic circulation. J Clim 14(10):2266–2280
757 Enfield DB, Mestas-Nuñez AM, Trimble PJ (2001) The Atlantic multidecadal oscillation and
758 its relation to rainfall and river flows in the continental US. Geophys Res Lett 28(10):2077–
759 2080
760 Fanning AF, Weaver AJ (1998) Thermohaline variability: The effects of horizontal resolution
761 and diffusion. J Clim 11(4):709–715
762 Ferreira D, Marshall J, Campin JM (2010) Localization of deep water formation: Role of
763 atmospheric moisture transport and geometrical constraints on ocean circulation. J Clim
764 23(6):1456–1476
765 Folland C, Palmer T, Parker D (1986) Sahel rainfall and worldwide sea temperatures, 1901–85.
766 Nature 320(6063):602–607
767 Frankcombe L, Dijkstra H (2009) Coherent multidecadal variability in North Atlantic sea level.
768 Geophys Res Lett 36(L15604)
769 Frankcombe L, Dijkstra H, Von der Heydt A (2008) Sub-surface signatures of the Atlantic
770 Multidecadal Oscillation. Geophys Res Lett 35(L19602)

771 Frankcombe LM, Dijkstra HA, Von der Heydt A (2009) Noise-induced multidecadal variability
772 in the North Atlantic: Excitation of normal modes. J Phys Oceanogr 39(1):220–233
773 Frankcombe LM, Von Der Heydt A, Dijkstra HA (2010) North Atlantic multidecadal climate
774 variability: an investigation of dominant time scales and processes. J Clim 23(13):3626–3638
775 Frankignoul C, Hasselmann K (1977) Stochastic climate models, part ii application to sea-
776 surface temperature anomalies and thermocline variability. Tellus 29(4):289–305
777 Frankignoul C, Czaja A, L'Heveder B (1998) Air-sea feedback in the North Atlantic and surface
778 boundary conditions for ocean models. J Clim 11(9):2310–2324
779 Gastineau G, Frankignoul C (2012) Cold-season atmospheric response to the natural variability
780 of the Atlantic meridional overturning circulation. Clim Dyn 39(1-2):37–57
781 Gent PR, McWilliams JC (1990) Isopycnal mixing in ocean circulation models. J Phys
782 Oceanogr 20(1):150–155
783 Griffies SM, Tziperman E (1995) A linear thermohaline oscillator driven by stochastic atmo-
784 spheric forcing. J Clim 8:2440–2453
785 Gulev SK, Latif M, Keenlyside N, Park W, Koltermann KP (2013) North Atlantic Ocean
786 control on surface heat flux on multidecadal timescales. Nature 499(7459):464–467
787 Harnik N, Chang EK (2004) The effects of variations in jet width on the growth of baroclinic
788 waves: Implications for midwinter Pacific storm track variability. J Atmos Sci 61(1):23–40
789 Hirschi J, Marotzke J (2007) Reconstructing the meridional overturning circulation from
790 boundary densities and the zonal wind stress. J Phys Oceanogr 37(3):743–763
791 Hodson DL, Sutton RT (2012) The impact of resolution on the adjustment and decadal vari-
792 ability of the Atlantic meridional overturning circulation in a coupled climate model. Clim
793 Dyn 39(12):3057–3073
794 Huck T, Vallis GK, Colin de Verdière A (2001) On the robustness of the interdecadal modes
795 of the thermohaline circulation. J Clim 14(5):940–963
796 Huck T, Arzel O, Sévellec F (2015) Multidecadal variability of the overturning circulation in
797 presence of eddy turbulence. J Phys Oceanogr 45(1):157–173
798 Hurrell JW (1995) Decadal trends in the North Atlantic Oscillation: regional temperatures
799 and precipitation. Science 269(5224):676–679

800 Kerr RA (2000) A North Atlantic climate pacemaker for the centuries. Science 288(5473):1984–
801 1985
802 Knight JR, Allan RJ, Folland CK, Vellinga M, Mann ME (2005) A signature of persistent
803 natural thermohaline circulation cycles in observed climate. Geophys Res Lett 32(L20708)
804 Kushnir Y (1994) Interdecadal variations in North Atlantic sea surface temperature and asso-
805 ciated atmospheric conditions. J Clim 7(1):141–157
806 Kushnir Y, Robinson WA, Blad I, Hall NMJ, Peng S, Sutton R (2002) Atmospheric gcm
807 response to extratropical sst anomalies: synthesis and evaluation. J Clim 15:2233–2256
808 Liu Z (2012) Dynamics of Interdecadal Climate Variability: A Historical Perspective*. J Clim
809 25(6):1963–1995
810 Marsh R, de Cuevas BA, Coward AC, Jacquin J, Hirschi JJM, Aksenov Y, Nurser A, Josey
811 SA (2009) Recent changes in the North Atlantic circulation simulated with eddy-permitting
812 and eddy-resolving ocean models. Ocean Model 28(4):226–239
813 Marshall J, Adcroft A, Hill C, Perelman L, Heisey C (1997) A finite-volume, incompress-
814 ible Navier Stokes model for studies of the ocean on parallel computers. J Geophys Res
815 102(C3):5753–5766
816 McCarthy GD, Haigh ID, Hirschi JJM, Grist JP, Smeed DA (2015) Ocean impact on decadal
817 Atlantic climate variability revealed by sea-level observations. Nature 521(7553):508–510
818 Mecking J, Keenlyside NS, Greatbatch RJ (2014) Stochastically-forced multidecadal variability
819 in the north atlantic: a model study. Clim Dyn 43:271–288
820 Minobe S, Kuwano-Yoshida A, Komori N, Xie SP, Small RJ (2008) Influence of the gulf stream
821 on the troposphere. Nature 452(7184):206–209
822 Molteni F (2003) Atmospheric simulations using a GCM with simplified physical parametriza-
823 tions. I: Model climatology and variability in multi-decadal experiments. Clim Dyn 20(2-
824 3):175–191
825 Ollitrault M, Colin de Verdière A (2002) SOFAR floats reveal midlatitude intermediate
826 North Atlantic general circulation. Part II: An Eulerian statistical view. J Phys Oceanogr
827 32(7):2034–2053
828 Ortega P, Mignot J, Swingedouw D, Sévellec F, Guilyardi E (2015) Reconciling two alternative
829 mechanisms behind bi-decadal AMOC variability. Prog Oceanogr (in revision)

Penduff T, Juza M, Barnier B, Zika J, Dewar WK, Treguier AM, Molines JM, Audiffren N (2011) Sea level expression of intrinsic and forced ocean variabilities at interannual time scales. J Clim 24(21):5652–5670

Pope V, Stratton R (2002) The processes governing horizontal resolution sensitivity in a climate model. Clim Dyn 19(3-4):211–236

Redi MH (1982) Oceanic isopycnal mixing by coordinate rotation. J Phys Oceanogr 12(10):1154–1158

Schlesinger ME, Ramankutty N (1994) An oscillation in the global climate system of period 65-70 years. Nature 367(6465):723–726

Sévellec F, Fedorov AV (2013) The leading, interdecadal eigenmode of the Atlantic meridional overturning circulation in a realistic ocean model. J Clim 26(7):2160–2183

Sévellec F, Huck T (2015) Theoretical Investigation of the Atlantic Multidecadal Oscillation. J Phys Oceanogr (2015)

Sévellec F, Huck T, Ben Jelloul M, Vialard J (2009) Nonnormal multidecadal response of the thermohaline circulation induced by optimal surface salinity perturbations. J Phys Oceanogr 39(4):852–872

Skyllingstad ED, Vickers D, Mahrt L, Samelson R (2007) Effects of mesoscale sea-surface temperature fronts on the marine atmospheric boundary layer. Bound Layer Meteorol 123(2):219–237

Sun C, Li J, Jin FF (2015) A delayed oscillator model for the quasi-periodic multidecadal variability of the NAO. Clim Dyn pp 1–17

Sutton RT, Hodson DL (2005) Atlantic Ocean forcing of North American and European summer climate. Science 309(5731):115–118

Te Raa LA, Dijkstra HA (2002) Instability of the thermohaline ocean circulation on interdecadal timescales. J Phys Oceanogr 32(1):138–160

Thompson DW, Wallace JM (1998) The arctic oscillation signature in the wintertime geopotential height and temperature fields. Geophys Res Lett 25(9):1297–1300

Thompson DW, Wallace JM (2001) Regional climate impacts of the Northern Hemisphere annular mode. Science 293(5527):85–89

Timmermann A, Latif M, Voss R, Grötzner A (1998) Northern hemispheric interdecadal variability: a coupled air-sea mode. J Clim 11(8):1906–1931

Trenberth K, Caron J, Stepaniak D (2001) The atmospheric energy budget and implications for surface fluxes and ocean heat transports. Clim Dyn 17(4):259–276

Tulloch R, Marshall J (2012) Exploring mechanisms of variability and predictability of Atlantic meridional overturning circulation in two coupled climate models. J Clim 25(12):4067–4080

Vallis GK, Gerber EP, Kushner PJ, Cash BA (2004) A mechanism and simple dynamical model of the North Atlantic Oscillation and annular modes. J Atmos Sci 61(3):264–280

Weaver AJ, Valcke S (1998) On the variability of the thermohaline circulation in the GFDL coupled model. J Clim 11(4):759–767

Winton M (1997) The damping effect of bottom topography on internal decadal-scale oscillations of the thermohaline circulation. J Phys Oceanogr 27(1):203–208

Zhang R (2008) Coherent surface-subsurface fingerprint of the Atlantic meridional overturning circulation. Geophys Res Lett 35(L20705)

Zhang R (2010) Latitudinal dependence of Atlantic meridional overturning circulation (AMOC) variations. Geophys Res Lett 37(L16703)

Table 1 Main characteristics of oceanic and atmospheric components of the Double Drake configuration at three different resolutions. From left to right: name of the set-up, horizontal resolution (in °), oceanic and atmospheric time step (s), transfer coefficient for eddy-induced advection and diffusion processes ($m^2\ s^{-1}$), horizontal viscosity ($m^2\ s^{-1}$), time integration (yr), and standard deviation σ of yearly MOC and NAM indices. The latter is computed with the absolute maximum of the spatial EOF1 pattern obtained with a projection onto the standardized PC1. The first EOF/PC is computed on the yearly SLPA over the north hemisphere only

model	Δx	Δt		Ocn GM	ν_{ocn}	Integration	σ_{MOC}	σ_{NAM}
set-up	(deg)	Ocn (s)	Atm (s)	($m^2\ s^{-1}$)	($m^2\ s^{-1}$)	(yr)	(Sv)	(hPa)
cs24	$\sim 3.8°$	3600	1200	1200	3.10^5	600	0.95	2.98
cs48	$\sim 1.9°$	2400	400	1200	1.10^5	600	1.76	4.13
cs96	$\sim 0.9°$	2400	200	1200	4.10^4	600	1.91	5.39

Table 2 Correlation between the yearly MOC index of Buckley et al (2012), defined as the average of the small basin MOC in the box [8°-60°N, 460-1890 m depth] (black box in Fig. 2, bottom panels), and 8 other yearly time series related to the overturning: 1/ a western boundary velocity index (WBC, defined as meridional velocities anomaly along the western boundary at 30°N, averaged in the upper 1000 m), 2/ the maximum of the MOC within the box [8°-60°N, 460-1890 m depth] (allowing spatial variations of its location (Marsh et al, 2009)), 3/ the Principal Component (PC) of the first Empirical Orthogonal Function (EOF) of the MOC streamfunction within the small basin, north of 34°S (explaining more than 60% of the variance) and 4/ the maximum of the mean MOC at 5 given latitudes (21°N, 30°N, 42°N, 50°N and 63°N). At 63°N, the MOC is in advance of a couple of years compared to the initial MOC index, as illustrated on Fig. 8 of Buckley et al (2012) for cs24. This lag between MOC anomalies at various latitudes explains the lower correlation found at high latitudes. In addition, all latitudes from 8-60°N are integrated into the original MOC index, while the MOC variability at 63°N is not considered

	WBC	MOC_{max}	PC_1^{moc}	MOC_{21N}	MOC_{30N}	MOC_{42N}	MOC_{50N}	MOC_{63N}
cs24	$r = 0.80$	0.91	0.99	0.91	0.90	0.91	0.80	0.37
cs48	$r = 0.80$	0.98	0.99	0.98	0.97	0.97	0.95	0.76
cs96	$r = 0.80$	0.97	0.97	0.97	0.97	0.96	0.96	0.77

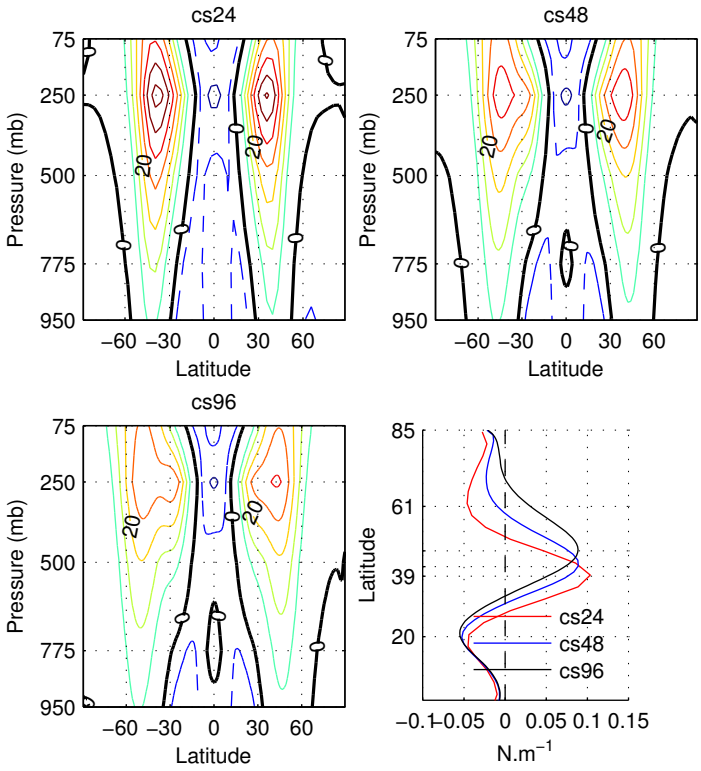

Fig. 1 Zonal mean zonal winds for cs24 (top left), cs48 (top right) and cs96 (bottom left). The contour interval is 5 m s^{-1}, negative values are dashed lines, and the zero contour is thick black line. (bottom right) Zonal surface wind stress zonally averaged over the small basin. Maximum of the eastward surface wind stress is at 39°N, 42°N and 47°N for cs24, cs48 and cs96, respectively. Extrema for cs24 are labelled on the y axis

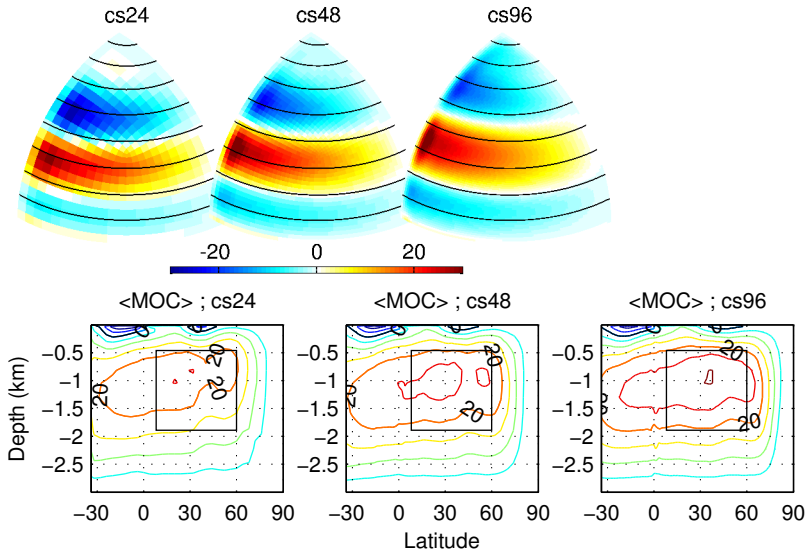

Fig. 2 (top panels) Barotropic streamfunction in Sv (1 Sv=10^6 m^3 s^{-1}) within the small basin flat-bottom ocean; thin black contours mark latitude circles every 10° from 10°N to 80°N. (bottom panels) Meridional Overturning Circulation (MOC) in Sv within the small basin; the black box represents the region [8°-60°N; 460-1890 m depth] used to define the MOC index. The contour interval is 5 Sv and the zero contour is black. All fields are time mean over the last 400 yr of integrations

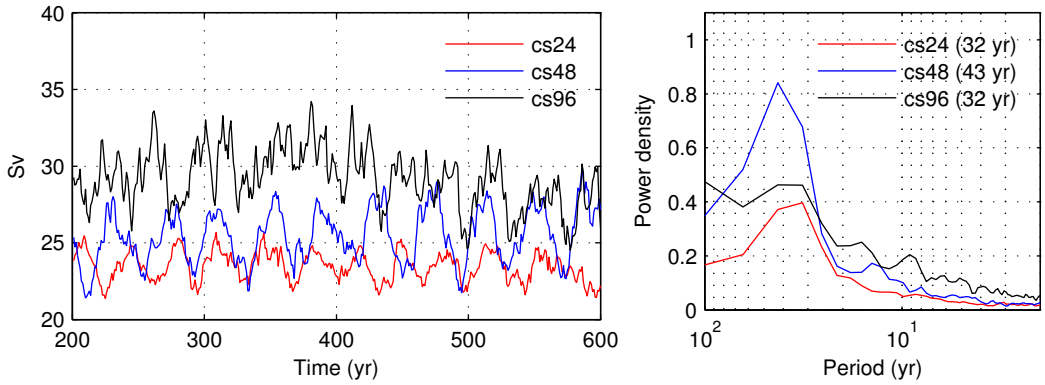

Fig. 3 Yearly MOC time series in the box [8°-60°N; 460-1890m] (black box on Fig 2, bottom panels; see text for details) in Sv for all three set-ups (left) and their respective power spectrum (right). The time scale of the dominant period for each time series is displayed on the right panel.

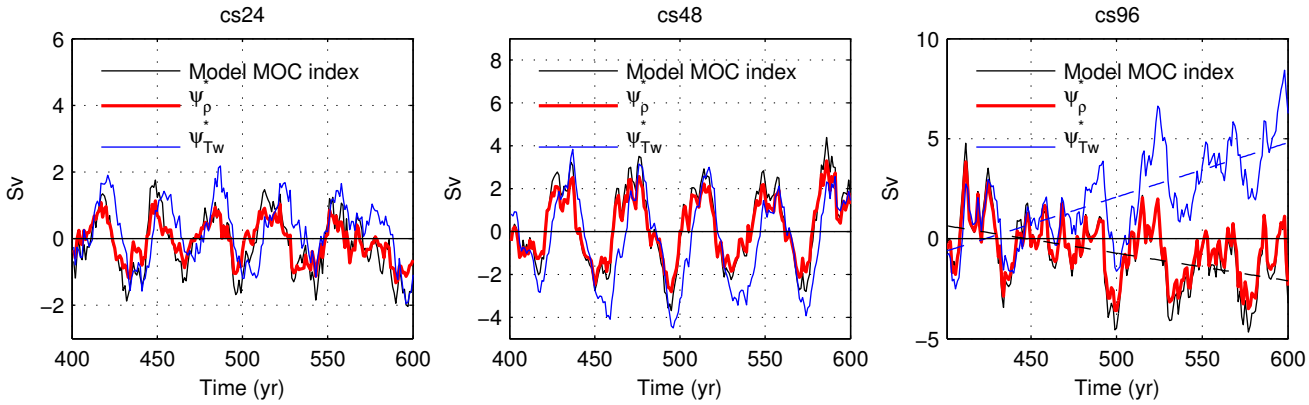

Fig. 4 Reconstruction of the MOC index (model, black line) using the thermal wind relationship with density anomalies along eastern and western boundaries (ψ^*_ρ, red) and temperature anomalies along the western boundary ($\psi^*_{T_w}$, blue) for cs24 (left), cs48 (centre) and cs96 (right). See Appendix 2 for details. For cs24 (respectively cs48, cs96), the correlation is $r = 0.92$ (0.99, 0.99) and 0.66 (0.82, 0.78) for the MOC index reconstructed from ψ^*_ρ and $\psi^*_{T_w}$, respectively. To compute the skill/correlation related to $\psi^*_{T_w}$, both the model and reconstructed MOC indices have been linearly detrended for cs96 (black and blue dashed lines on the right panel).

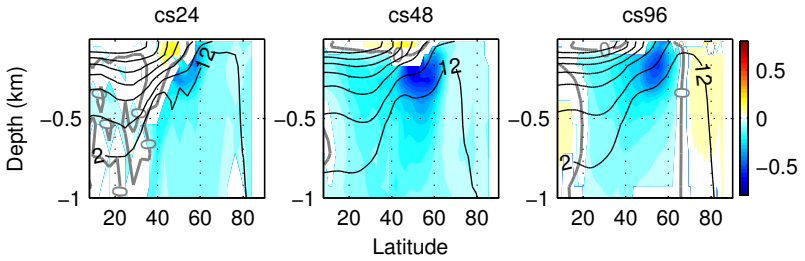

Fig. 5 Yearly temperature anomalies along the western boundary (K) in the upper 1500 m associated with one standard deviation of the yearly MOC index at lag=0, for cs24 (left), cs48 (centre) and cs96 (right). Regions that are not statistically significant at 5% level are white shaded, and the zero regression is thick grey line. Black contours represent the mean potential temperature along the boundary. Contour interval is 3 K

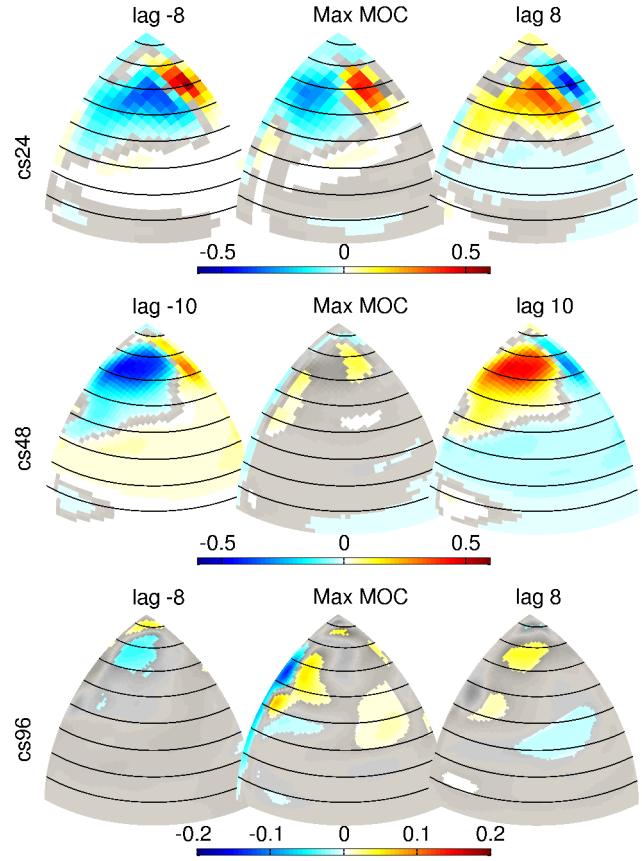

Fig. 6 Yearly oceanic potential temperature anomalies averaged over the upper 1000 m (T1000, in K) associated with one standard deviation of the yearly MOC index for cs24 (top row panels), cs48 (middle row) and cs96 (bottom row). Center panels correspond to $lag = 0$, while left (right) panels correspond to $lag = -\frac{1}{4}T$ ($lag = +\frac{1}{4}T$), with T the dominant period of the MOC variability estimated from the MOC index power spectrum (i.e., 32 yr for both cs24 and cs96, 43 yr for cs48). $lag = -\frac{1}{4}T$ ($lag = +\frac{1}{4}T$) corresponds to a strengthening (weakening) MOC. Regions that are not statistically significant at the 5% level are grey shaded (see Appendix 1 for details). Thin black contours mark latitude circles every 10° from 10°N to 80°N. Note the different colour axis for cs96

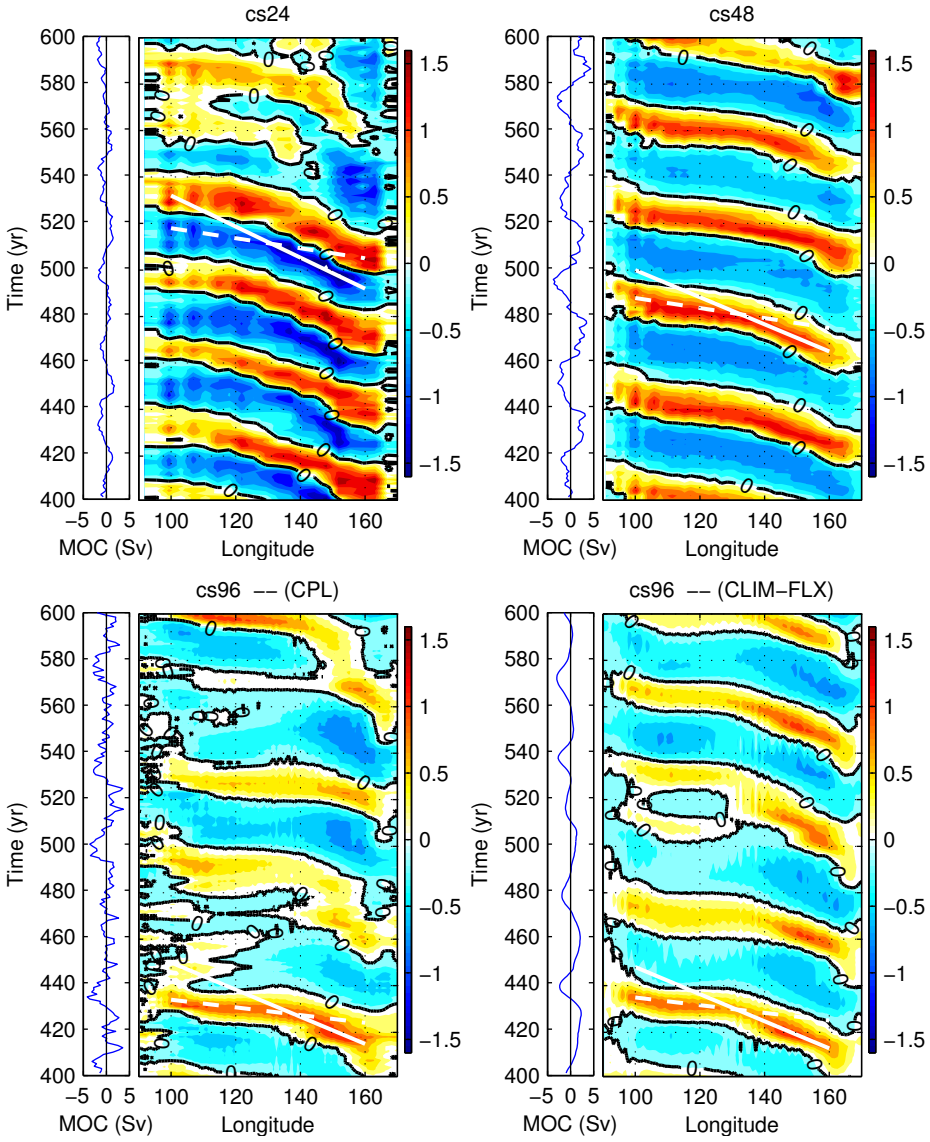

Fig. 7 Hovmöller diagrams of yearly potential temperature anomalies in the thermocline (in K) for the last 200 yr of simulation for coupled runs cs24 (top left), cs48 (top right), cs96 (bottom left) and the forced run CLIM-FLX of cs96 (bottom right). The east-west cross section is computed between 55°-65°N, 60°-70°N and 65°-75°N for cs24, cs48 and for both cs96 runs respectively, and at the depth of the maximum anomalies, i.e. 265 m for cs24 and 540 m for cs48 and cs96 runs. The zero contour is thick black line. Continuous (dashed) white lines show an estimate of the westward phase velocity of temperature anomalies across the eastern (western) half of the small basin. The corresponding MOC index is shown on the left of each diagram

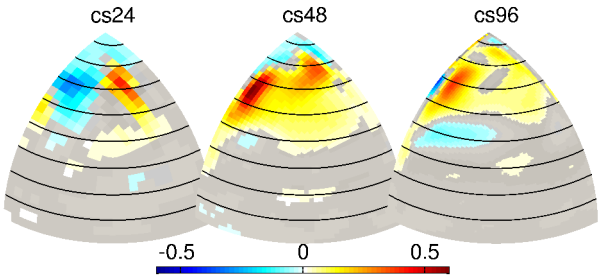

Fig. 8 Yearly Sea Surface Temperature (SST) anomalies (K) associated with one standard deviation of the yearly MOC index at lag=0, for cs24 (left), cs48 (centre) and cs96 (right). Regions that are not statistically significant at the 5% level are grey shaded. The thin black contours mark latitude circles every 10° from 10°N to 80°N

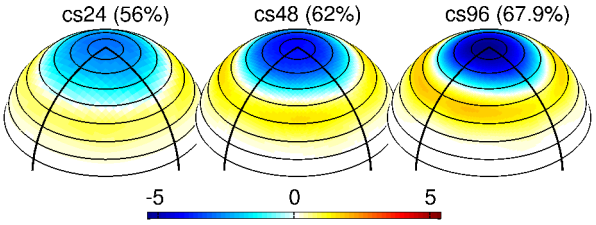

Fig. 9 First EOF of the yearly Sea Level Pressure Anomaly (SLPA, in hPa) in the northern hemisphere. The explained variance is displayed at the top of each plots. The EOFs are normalized by the standard deviation of their corresponding PC. The thin black contours mark latitude circles every 10° from 10°N to 80°N, and the thick orthogonal black lines the boundaries of the small basin

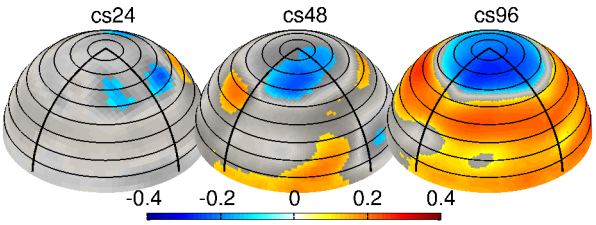

Fig. 10 Correlation between yearly Sea Level Pressure and the yearly MOC index 2 yr later (i.e. when the most significant correlations are found). Regions that are not statistically significant at the 5% level are grey shaded. The thin black contours mark latitude circles every 10° from 10°N to 80°N, and the thick orthogonal black lines the boundaries of the small basin

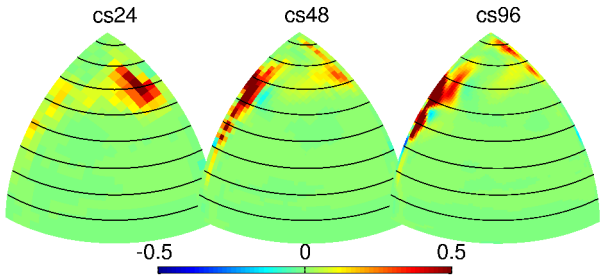

Fig. 11 Term $-\overline{\mathbf{u}'T'}\boldsymbol{\nabla}\overline{T}$ related to baroclinic instability eddy fluxes in the potential temperature variance budget averaged over the upper 1000 m ocean and over several MOC oscillation periods, in K^2 yr^{-1}. The thin black contours mark latitude circles every 10° from 10°N to 80°N

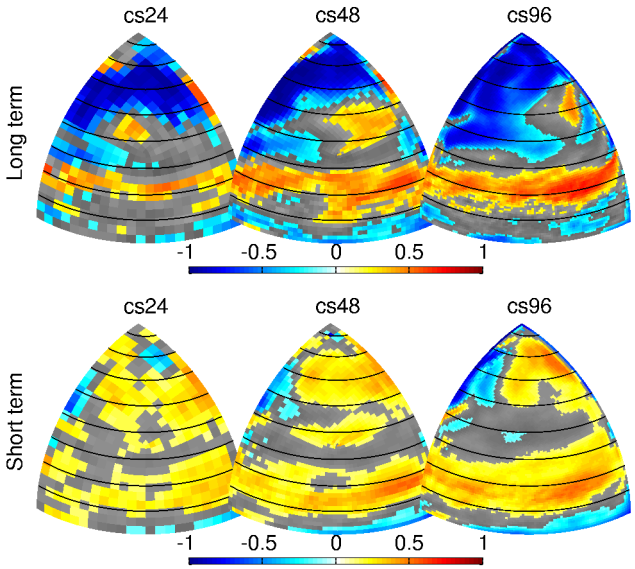

Fig. 12 Correlation between Sea Surface Temperature (SST) anomalies and the ocean-atmosphere heat fluxes (Q, positive downward for a release of heat into the ocean) for the multidecadal signal - 10 yr running mean - (top) and interannual signal - residual variability of the 10 yr running mean - (bottom). Regions that are not statistically significant at the 5% level are grey shaded. The thin black contours mark latitude circles every 10° from 10°N to 80°N

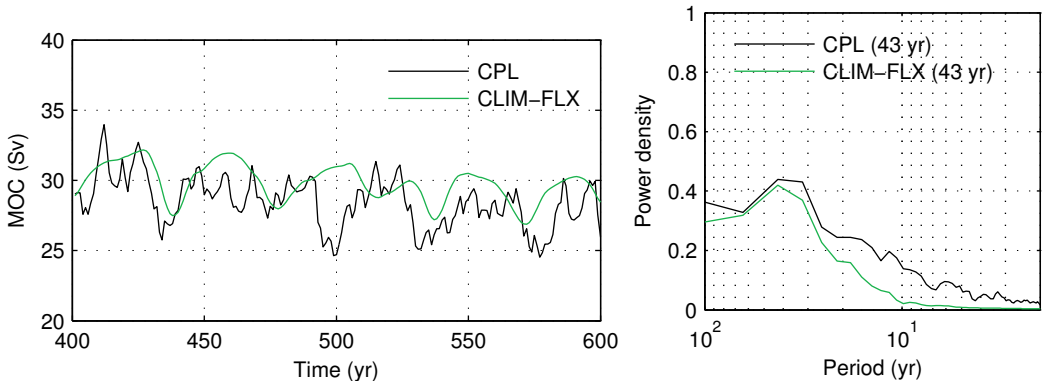

Fig. 13 Yearly MOC time series (left) and respective power spectra (right) for the coupled configuration (CPL, black) and the ocean-only configuration forced by climatological fluxes and SST restoring toward climatological values (CLIM-FLX, green) for cs96. The time scale of the dominant period of each time series is displayed on the right panel, the difference with Fig. 3 results from the shorter time series used for the spectrum